

Energy Transfers and Reflection of Infragravity Waves at a Dissipative Beach Under Storm Waves

Xavier Bertin¹ , Kévin Martins^{1,2} , Anouk de Bakker^{1,3} , Teddy Chataigner^{1,4}, Thomas Guérin^{1,5} , Thibault Coulombier¹, and Olivier de Viron¹ 

¹UMR 7266 LIENSs CNRS-La Rochelle Université, La Rochelle, France, ²Now at UMR 5805 EPOC, CNRS-University of Bordeaux, Bordeaux, France, ³Now at Unit of Marine and Coastal Systems, Deltares, Delft, Netherlands, ⁴Now at Laboratoire Saint Venant, Sorbonne University, Paris, France, ⁵Now at SAS Benoit Waeles - Consultant Génie Côtier, Brest, France

Key Points:

- Very large IG waves are observed at a dissipative beach under a storm, long-period swell and are driven by the bound wave mechanism
- In the surf zone, IG wave energy is transferred not only toward superharmonic but also toward subharmonic frequencies
- IG wave reflection is tidally modulated and almost full at high tide due to the increase in beach slope

Correspondence to:

X. Bertin,
xbertin@univ-lr.fr

Citation:

Bertin, X., Martins, K., de Bakker, A., et al. (2020). Energy transfers and reflection of infragravity waves at a dissipative beach under storm waves. *Journal of Geophysical Research: Oceans*, 125, e2019JC015714. <https://doi.org/10.1029/2019JC015714>

Received 30 SEP 2019

Accepted 9 APR 2020

Accepted article online 20 APR 2020

Abstract This study presents unpublished field observations of infragravity waves, collected at the dissipative beach of Saint-Trojan (Oléron Island, France) during the storm Kurt (3 February 2017), characterized by incident short waves of significant heights reaching 9.5 m and peak periods reaching 22 s. Data analysis reveals the development of exceptionally large infragravity waves, with significant heights reaching 1.85 m close to shore. Field observations are complemented by numerical modeling with XBeach, which well reproduces the development of such infragravity waves. Model results reveal that infragravity waves were generated mainly through the bound wave mechanism, enhanced by the development of a phase lag with the shortwave energy envelope. Spectral analysis of the free surface elevation shows the generation of superharmonic and subharmonic infragravity waves, the latter dominating the free surface elevation variance close to shore. Modeling results suggest that subharmonic infragravity waves result, at least partly, from infragravity-wave merging, promoted by the combination of free and bound infragravity waves propagating across a several kilometer-wide surf zone. Due to the steeper slope of the upper part of the beach profile, observed and modeled reflection coefficients under moderate-energy show a strong tidal modulation, with a weak reflection at low tide ($R^2 < 0.2$) and a full reflection at high tide ($R^2 \sim 1.0$). Under storm waves, the observed reflection coefficients remain unusually high for a dissipative beach ($R^2 \sim 0.5 - 1.0$), which is explained by the development of subharmonic infragravity waves with frequencies around 0.005 Hz, too long to suffer a substantial dissipation.

1. Introduction

Infragravity (hereafter IG) waves are surface gravity waves with frequencies typically ranging from 0.004 to 0.04 Hz, related to the presence of groups in incident shortwaves (see Bertin et al., 2018 for a recent review). IG waves are only a few mm to cm high in the deep ocean (e.g., Crawford et al., 2015; Rawat et al., 2014; Smit et al., 2018) but can exceed 1.0 m close to shore under storm conditions (Inch et al., 2017; Fiedler et al., 2015; Ruessink, 2010). Although not validated against field observations, the application of XBeach (Roelvink et al., 2009) to the SW of Oléron Island (France) by Baumann et al. (2017) even suggests that IG waves could exceed 2.0 m close to shore under very energetic, narrow-banded incident swells. Therefore, IG waves have an essential contribution to sandy beach (e.g., Guza & Thornton, 1982; Elgar et al., 1992; Ruessink et al., 1998; Reniers et al., 2002; Guedes et al., 2013) and tidal inlet hydrodynamics (Bertin & Olabarrieta, 2016; Bertin et al., 2019; Mendes et al., 2020), sediment transport (e.g., Russell, 1993; Aagaard & Greenwood, 2008; De Bakker et al., 2016), and dune and barrier breaching (e.g., Roelvink et al., 2009), particularly under storm waves.

At dissipative beaches, IG waves usually dominate the spectrum of the free surface elevation close to shore (Guza & Thornton, 1982; Russell, 1993; Ruessink et al., 1998) and therefore control the development of large runup (Raubenheimer & Guza, 1996; Ruessink et al., 1998; Ruggiero et al., 2001) and overwash along the coast and subsequent washovers in low-lying zones (e.g., Baumann et al., 2017). At such gently sloping beaches, IG waves are mostly generated through the bound wave mechanism, which corresponds to second-order nonlinear wave-wave interactions that result in the development of long waves, out of phase with the energy envelope of the shortwaves. This mechanism was first demonstrated analytically in 1-D by Biesel (1952) and Longuet-Higgins and Stewart (1962) and was then extended to 2-D random waves by

Hasselmann (1962). These analytical solutions imply that the frequency of the resulting IG waves should decrease under narrow-banded and long-period incident short waves. Yet, Bertin and Olabarrieta (2016) observed relatively short-period IG waves (e.g., $T < 60$ s) under such incident short waves while other authors reported IG wave periods in the range 120–300 s under shorter period incident waves (e.g., De Bakker et al., 2014; Inch et al., 2017). This apparent inconsistency suggests that the relationship between the shape of the incident shortwave spectra and the frequency of IG waves is not straightforward. Also, these analytical solutions were derived considering a flat bottom while for sloping bottoms, the bound waves increasingly lag behind the wave groups as and when the water depth decreases. This phase lag was observed in both field (e.g., List, 1992; Masselink, 1995; Inch et al., 2017) and laboratory experiments (Battjes et al., 2004; De Bakker et al., 2013; Padilla & Alsina, 2017) and was demonstrated semi-analytically (Janssen et al., 2003; Guérin et al., 2019). Van Dongeren et al. (2007) showed that the presence of this phase lag enhances energy transfer from short waves to IG waves. This process is often referred to as “bound wave shoaling,” which is somehow misleading because the resulting growth of IG waves is higher than the growth associated with conservative shoaling (i.e., Green’s Law).

In the surf zone, depth-induced breaking of shortwaves results in a shoreward reduction of shortwave groupiness, which allows for the release of IG waves that then propagate as free waves (e.g., Janssen et al., 2003; Battjes et al., 2004; Janssen et al., 2003). Baldock (2012) proposed that bound wave release can only occur if short waves are in the shallow-water regime when breaking, which condition is not necessarily met under short period waves and/or storm conditions. Throughout their propagation in the inner surf zone of gently sloping beaches, IG waves transfer energy to higher frequencies and steepen, which promotes their dissipation through depth-limited breaking (Battjes et al., 2004; Lin & Hwung, 2012; De Bakker et al., 2014). Several authors reported the saturation of wave runup in the IG band under storm waves (Ruessink et al., 1998; Ruggiero et al., 2004; Sénéchal et al., 2011), possibly owing to IG wave dissipation close to shore. However, Fiedler et al. (2015) did not observe any runup saturation under comparable incident conditions and beach slope, suggesting that further research on IG wave dissipation is needed. IG wave energy that is not dissipated in the surf zone can be reflected along the shore, a process that was observed and quantified both in the field (Huntley et al., 1981; Guza & Thornton, 1985; Elgar et al., 1994; De Bakker et al., 2014; Inch et al., 2017) and in laboratory experiments (Battjes et al., 2004; Van Dongeren et al., 2007). The reflection coefficient R^2 , which corresponds to the ratio between the outgoing and the incoming IG wave energy, was shown to increase with the beach slope and with the period of incident IG waves (Van Dongeren et al., 2007). As sandy beaches often exhibit steeper slopes in their upper part, a tidal modulation of IG wave reflection is expected and was already reported (Okiihiro & Guza, 1995). Recent observations of free IG waves across the shelf of Oregon even revealed that such a tidal modulation can be strong in the deep ocean (Smit et al., 2018). The frequency dependence of IG wave dissipation and reflection processes produces large differences in the cross-shore structure of surface elevation spectra. Indeed, higher-frequency IG waves tend to be progressive across the surf zone while lower frequencies tend to develop quasi-standing patterns due to a stronger reflection (De Bakker et al., 2014; Inch et al., 2017).

In a recent review paper, Bertin et al. (2018) pointed out that further research on IG waves was needed to better understand their generation mechanisms, their transformations across the surf zone, and their reflection along the coast. This study aims to contribute to this effort and to answer more specifically the following questions: How large can IG waves be in the nearshore? What is the relationship between the shape of the incident shortwave spectra and the IG waves spectra along the coast? Do IG waves necessarily suffer strong dissipation and subsequent low reflection at a dissipative beach? To address these questions, we present the analysis of an unpublished data set collected under storm wave conditions at a dissipative beach located to the SW of Oléron island (France), complemented with numerical modeling using XBeach (Roelvink et al., 2009).

2. Study Area

This study takes place at Saint-Trojan Beach, a dissipative beach located in the central part of the French Atlantic coast (Figure 1), along the southwestern coast of Oléron Island. This stretch of coast corresponds to a 8 km-long sandspit, bounded to the South by the Maumusson Inlet (Bertin et al., 2005). The continental shelf in front of the study area is about 150 km wide, with a very gently sloping shoreface, the isobath 20 m being found about 10 km away from the shoreline. The tidal regime in this region is semidiurnal and macrotidal, with a tidal range varying between about 1.5 m during neap tides and 5.5 m during spring tides.

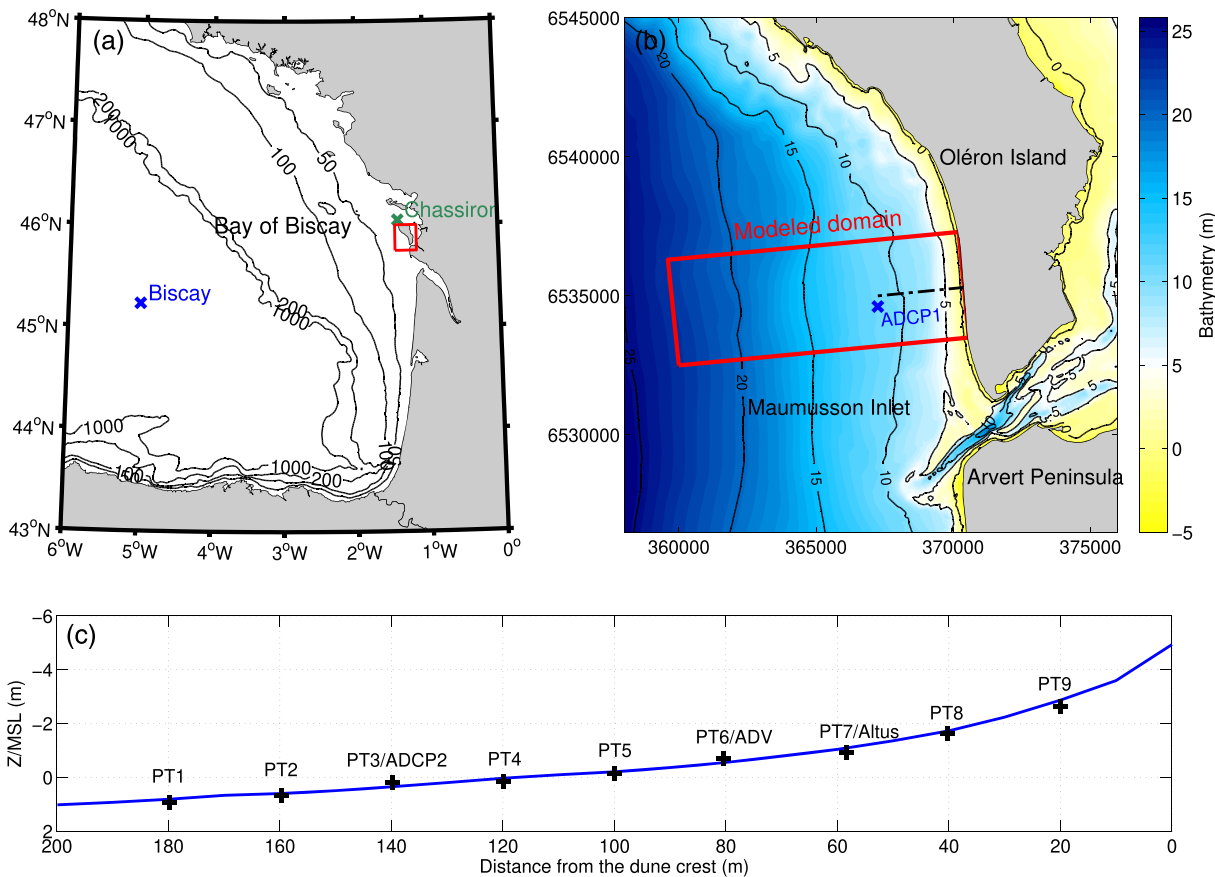


Figure 1. (a) Location of the study area in the Bay of Biscay, with the Biscay buoy (x) and Chassiron Meteorological station (x). (b) Detailed bathymetry of the study area (m relative to mean sea level), showing the location of the offshore ADCP1 (x) and the instrumented cross-shore profile (dashed line). The coordinates are in meter (Lambert-93 projection). (c) Zoom-in on the intertidal part of the instrumented cross-shore profile, showing the location of the instruments used in this study (+) with respect to the beach topography (blue line).

Tidal currents remain weak at the studied beach, and the impact of tides on short waves remains mostly restricted to water level variations. According to Bertin et al. (2008), yearly-mean deep water wave conditions are characterized by a significant height (H_s) of 2 m, a peak period (T_p) of 10 s, and a mean direction of 285° N. During storms, H_s can reach episodically 10 m in deep water and T_p can exceed 20 s with a westerly direction (Bertin et al., 2015). Due to the very gently sloping shoreface and the wide continental shelf, the most energetic waves suffer strong dissipation, and numerical wave models suggest that their H_s hardly exceeds 5 m at the breaking point (Bertin et al., 2008).

The studied beach is mainly composed of fine and well-sorted sands ($d_{50} = 0.18\text{--}0.22$ mm), which together with the energetic wave climate and the macrotidal range cause its morphology to be non-barred and dissipative (Figure 1b). Small-amplitude intertidal bars can only develop after the persistence of fair weather conditions. Its slope typically ranges from about 0.0015 at the shoreface to 0.015 in the intertidal area (Bertin et al., 2008), although a berm usually develops during the course of the summer period, with a slope reaching 0.04. Due to the persistence of low to moderate-energy wave conditions in autumn 2016 and early winter 2017, such a berm was still present during our field campaign. This gently sloping morphology and the presence of a shallow shoreface induce a strong wave refraction, so that the wave angle at breaking is usually small, with typical values smaller than 10° (Bertin et al., 2008).

3. Field Campaign and Data Processing

The field campaign presented in this study was motivated by the development of the storm Kurt, which started to deepen to the SE of the Newfoundland on the 31 January 2017 and crossed the North Atlantic Ocean following an Eastward track, centered between 48° and 50° . Based on the CFSR reanalysis (Saha et al.,

2010), Kurt reached a minimum sea level pressure around 955 mbar on the 2 February 2017 about 1,000 km to the West of the Bay of Biscay, accompanied with a ~ 500 km-wide band of western winds in the range 25–35 m s⁻¹. This atmospheric setting drove a very large and long period swell, which reached the French coasts in the night of 2 February 2017 to 3 February 2017. At the deep water buoy of Biscay (Figure 1a), the mean wave period increased from 8.0 to 13.0 s, and H_s rapidly increased from 3.0 m to almost 10.0 m, which value corresponds to a return period on the order of 1 year (Nicolae-Lerma et al., 2015). The wave hindcast described in Guérin et al. (2018) suggests that the wave peak period T_p exceeded 20 s. The measurement period encompassed four tidal cycles, from 1 February 2017 to 3 February 2017, characterized by a tidal range of 3.5 to 4 m. An Acoustic Doppler Current Profiler (ADCP1) with a frequency of 600 kHz and equipped with a pressure sensor was deployed about 3 km offshore (Figure 1b). In the intertidal zone, nine pressure transducers (PT) sampling at 4 Hz were deployed (Figure 1c) as well as a second ADCP (ADCP2), with a head frequency of 2 MHz mounted with a pressure sensor at the location of PT3. The PTs were buried between 0.05 to 0.10 m of sand, in order to avoid dynamic pressure errors. The position of each sensor was measured with a differential GNSS, using a postprocessing technique with a base station settled on the dune crest in front of the instrumented profile (Guérin et al., 2018). This GNSS was also used to survey the intertidal beach topography at every low tide. The analysis of this data revealed surprisingly small morphological changes for storm wave conditions, typically lower than 0.1 m along the cross-shore profile of the instruments.

For each sensor, bottom pressure measurements were first corrected for sea level atmospheric pressure measured at the nearby meteorological station of Chassiron (Figure 1a). The entire record was split into consecutive bursts of 30 min, and only the bursts in which the sensor was continuously submerged were considered. PT9 was never continuously submerged for more than 30 min and data from this PT was therefore discarded for the present study. Bottom pressure power density spectra $E_p(f)$ were computed using Fast Fourier Transforms, with 10 Hanning windowed, 50% overlapping segments (20 degrees of freedom). These pressure spectra were then converted into elevation spectra $E(f)$ considering linear wave theory (see for instance Bishop & Donelan, 1987). The spectral significant wave height (H_{m0}) was computed as

$$H_{m0} = 4\sqrt{m_0} \quad (1)$$

with

$$m_0 = \int_{f_{min}}^{f_{max}} E(f)df, \quad (2)$$

where f_{max} was set to 0.4 Hz, a value for which the pressure correction reaches about 13 by 3 m water depth, well below the threshold of 100 to 1,000 recommended by Bishop and Donelan (1987). f_{min} is time-varying and defined following Roelvink and Stive (1989) or Hamm and Peronnard (1997) as half the continuous peak frequency f_p , computed from the offshore ADCP data as

$$f_p = \frac{m_0^2}{m_{-2} m_1}, \quad (3)$$

where

$$m_k = \int_{f_{min}}^{f_{max}} f^k E(f)df. \quad (4)$$

The continuous peak frequency was preferred to the discrete one because it is a more stable parameter, particularly under multimodal sea states, as it was the case at the beginning of the field campaign. As the incident peak period doubled during the field campaign, a fixed frequency cutoff would not have allowed for a proper separation between the gravity and the IG bands. In order to characterize the spatio-temporal variations of incoming IG wave frequencies, the mean IG wave period T_{m02,IG^+} was also computed based on the incoming IG wave signal, separated from the outgoing one at the ADCP2 and the ADV using the method of Guza et al. (1984):

$$T_{m02,IG^+} = \sqrt{\frac{m_0}{m_2}}. \quad (5)$$

4. Numerical Modeling

4.1. Model Description

XBeach is a two-dimensional modeling system that couples a Saint-Venant solver with a simplified wave-action model and a sediment transport model to simulate the generation and propagation of IG waves and the associated dynamics (Roelvink et al., 2009). Based on directional wave spectra provided along the open boundary, XBeach applies random phase summation to reconstruct time series of the free surface elevation. A Hilbert transform is applied to derive time series of short-wave energy varying at the scale of wave groups and imposed as boundary conditions in the wave action model. IG waves are represented explicitly in the Saint-Venant model and are forced by the gradient of wave radiation stress computed from the wave model. The incoming bound wave is computed following Herbers et al. (1994) and is imposed along the open boundary of the Saint-Venant model.

4.2. Model Implementation

A rectilinear grid centered on the instrumented cross-shore profile and extending 4,000 m in the alongshore direction was implemented. In the cross-shore direction, this grid starts from the dune crest and extends 11,000 m offshore, corresponding to a mean water depth of about 23 m (Figure 1b). The spatial resolution ranges from 20 m along the open boundary to 1 m in the beach upper part (Figure 1b). A sensitivity analysis revealed that such a fine resolution was required to adequately represent IG waves in shallow water and their reflection along the shoreline. Along the offshore open boundary, XBeach was forced with time-series of water levels recorded at ADCP1 (Figure 1b). The wave model was forced with time-series of directional wave spectra, originating from a regional application of the WaveWatchIII model (Tolman, 2009) forced by wind fields from the CFSR reanalysis (Saha et al., 2010). In deep water, Guérin et al. (2018) showed that this wave hindcast resulted in a normalized root mean squared discrepancy (hereafter NRMSD) of 10% for H_{m0} and 6% for the mean wave period. Bottom friction was represented by a quadratic bottom shear stress with a constant Chezy coefficient set to $80 \text{ m}^{0.5} \text{ s}^{-1}$. The horizontal eddy viscosity was assumed constant ($0.5 \text{ m}^2 \text{ s}^{-1}$), and the minimum water depth was set to 0.01 m. Depth-limited breaking in the wave model was represented using the model of Roelvink (1993a) with a breaking index γ adjusted to 0.38 after calibration. The model was run for the duration of the field experiment (3 days), and time-series of short wave height, surface elevation, and current velocities were archived at 2 Hz. In order to get insights into IG wave generation mechanisms, additional numerical experiments were performed, where wave forces were switched off either inside or outside the surf zone. The breaking formulation of Roelvink et al. (2009) was used to determine whether a computational node was located inside or outside the surf zone, that is, if the local wave height was not exceeding the threshold H_{max} as defined in Roelvink (1993b). In the bound wave case, wave forces were turned off inside the surf zone while in the breakpoint case, wave forces were turned off outside the surf zone, and the incoming boundwave was not included along the open boundary, following Pomeroy et al. (2012) and Bertin and Olabarrieta (2016). Lastly, additional 24 hr-long simulations were run with constant water levels and wave forcing at specific times of the measurement period to provide sufficient resolution and number of degrees of freedom for spectral and bispectral analysis used to investigate IG wave energy transfers through nonlinear triad coupling. Spectral estimates were computed following the same methodology as for the field observations (Section 3). Due to the random phase summation technique, a substantial scatter in terms of IG waves can be observed from one simulation to another. For model/data comparisons, bulk parameters computed from field observations were compared against the mean of a model ensemble of 10 realizations.

4.3. Model Postprocessing

Incoming and outgoing IG waves along the studied cross-shore profile were separated using a Radon transform (Radon, 1917). This technique projects the two-dimensional wave field (here space corresponds to the studied cross-shore profile and time to 1,800 s-long samples) into polar space (Yoo et al., 2011). The Radon transform is a powerful tool to study nearshore waves, as it allows the separation of incoming and outgoing wave fields on high-resolution data sets without any hypotheses on the hydrodynamics (e.g., Almar et al., 2014; Martins et al., 2017). The energy conservation properties of the method were assessed by examining the ratio of energy computed using the sum of the separated signals and that of the original total signal. The relative difference never exceeded 4% and was 1.4% on average over the simulated period. Reflection coefficients R^2 were computed as the ratio between the outgoing and the incoming IG wave energy.

In order to analyze IG-wave generation mechanisms, the phase lag between the shortwave energy envelope A and incoming IG waves η^+ was estimated using cross-spectral analysis:

$$\phi_{f,x} = \arctan \left[\frac{\mathcal{I}\{Cr_{A,\eta^+}(f,x)\}}{\mathcal{R}\{Cr_{A,\eta^+}(f,x)\}} \right], \quad (6)$$

where Cr is the cross-spectrum of the short wave envelope A and the incoming IG waves η_+ , separated along the studied cross-shore transect using the Radon transform described above and \mathcal{I} and \mathcal{R} are the imaginary and the real parts of the cross-spectrum. As this method provides a phase lag per frequency, the averaged values over the IG band (0.005–0.04 Hz) were considered, which eliminates the problem of selecting arbitrarily a single frequency while providing more stable phase lag estimates.

Possible energy transfers in the IG band were investigated through bispectral analysis, a technique originally introduced by Hasselmann et al. (1963) and then used in numerous IG wave studies (e.g., Elgar & Guza, 1985; De Bakker et al., 2015). Source terms for nonlinear energy transfers between frequencies S_{nl} were computed using the stochastic formulation of the second-order nonlinear wave interaction theory of Herbers et al. (2000):

$$S_{nl,f} = \frac{3\pi f}{h} \mathcal{I} \left\{ \left(\sum_{f'=0}^f \Delta f B_{f',f-f'} - 2 \sum_{f'=0}^{f_N-f} \Delta f B_{f',f} \right) \right\}, \quad (7)$$

where the term $\sum_{f'=0}^f B_{f',f-f'}$ represents the sum interactions in the imaginary part of the bispectrum B and the term $-2 \sum_{f'=0}^{\infty} B_{f',f}$ represents the difference interactions, as a particular frequency can contribute simultaneously to both difference and sum interactions. The 24-hr analyzed model samples allow computing these terms with 602 degrees of freedom and a spectral resolution of 0.0019 Hz. Further details on these analysis techniques can be found in Bertin et al. (2018).

5. Results

5.1. Characterization of Shortwaves and IG Wave Heights

As explained above, the field campaign presented in this study was motivated by the development of the storm Kurt, which generated offshore H_s of the order of 10.0 m with T_p over 20 s. At the ADCP1 (Figure 1a), the spectral significant wave height in the gravity band (hereafter $H_{m0,G}$) increased from 2.0 m at the beginning of the campaign to a maximum of 6.0 m on the 3 February 2017 (Figure 2b). Over the same period, T_p increased from 10–15 s to more than 20 s. The increase in $H_{m0,G}$ is well captured by XBeach, with a RMSD of 0.3 m and a NRMSD below 10%. In more detail, $H_{m0,G}$ is tidally modulated during the last tidal cycle, which suggests that the surf zone at low tide extended offshore of the ADCP1, located more than 3,000 m from the shoreline. At the sensors deployed in the intertidal zone (PT1 to PT9), wave heights were depth-limited and therefore strongly tidally-modulated, with $H_{m0,G}$ roughly equal to half of the water depth (Figure 3). Wave heights are well reproduced by XBeach, with a mean RMSD of 0.12 m over the eight intertidal sensors, which results in a NRMSD of 15% (Figure 4a). Gu erin et al. (2018) obtained slightly better predictions using an adaptive wave breaking parameterization, where the breaking index γ increases with the bottom slope. Such a parameterization is not available in XBeach and is in any case questionable for a spectral model resolving wave groups (e.g., Roelvink, 1993a).

Very large IG waves developed during the last tidal cycle, which corresponds to the arrival of the large swell generated by the storm Kurt. At the ADCP1 (Figure 1b), $H_{m0,IG}$ ranged from 0.25 to 0.5 m during the first three tidal cycles and increased to a maximum of 1.2 m (Figure 2), a value undocumented for a water depth of 13 m. $H_{m0,IG}$ are well reproduced by XBeach, except during the second tidal cycle, where an underestimation by a factor of 2 can be observed (Figure 2). In the intertidal zone, IG waves also increased from about 0.5 m during the first three tidal cycles to a maximum of 1.85 m at PT6, with individual IG waves exceeding 2.5 m (not shown). Figure 5 shows an example of time series of measured water depth at the ADCP2 (Figure 5a), where the low-pass filtered signal reveals that individual IG waves exceeded 2.0 m and induced cross-shore velocities ranging from -2.0 m s^{-1} (offshore) to $+2.0 \text{ m s}^{-1}$ (onshore) (Figure 5b). This figure also shows that alongshore velocities were much weaker (Figure 5c), with the ratio of the alongshore over the cross-shore IG velocity variance being lower than 10%. The extension of this analysis to the whole ADCP2 data set reveals this ratio is about $19 \pm 8\%$ (where \pm corresponds to one standard deviation), which means that the IG wave dynamics was dominated by cross-shore motions.

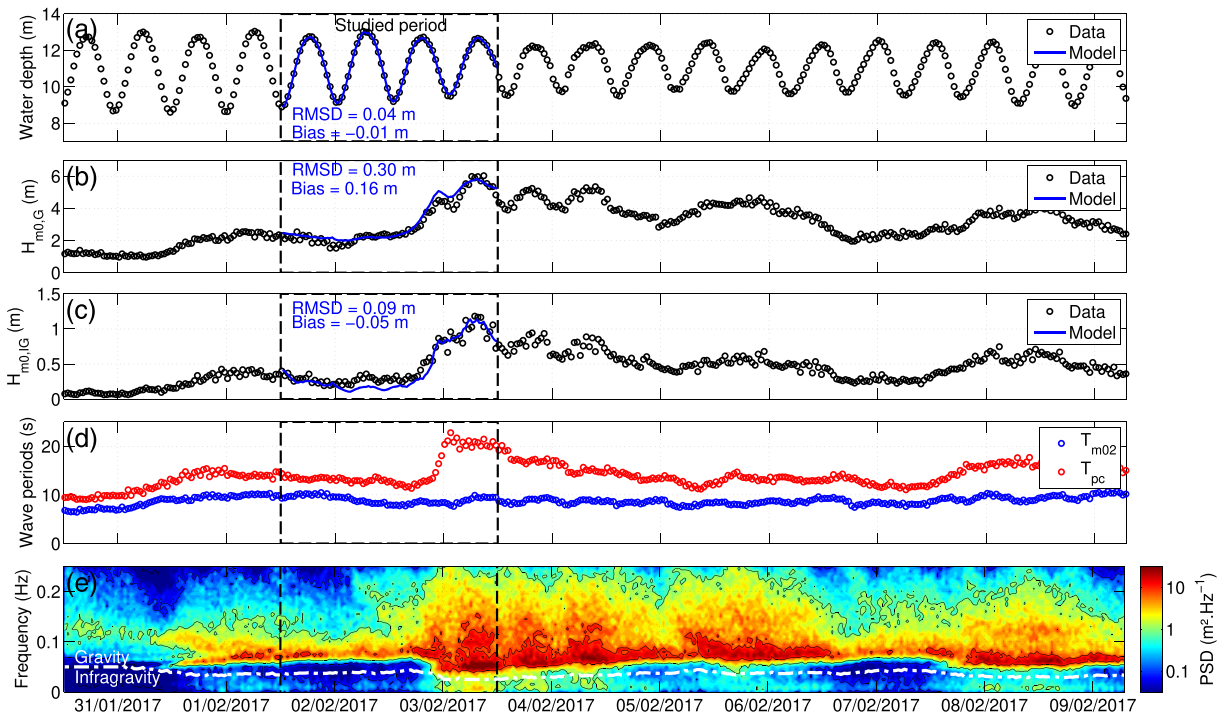


Figure 2. Time series of observed (circles) and modeled (solid lines) bulk parameters and spectra at the location of the ADCP1 (Figure 1b): (a) water depth; (b) H_{m0} in the gravity band; (c) H_{m0} in the IG band; (d) continuous peak (red) and mean (blue) wave periods, and (e) power density spectra of observed water levels computed, where the white dashed line corresponds to the adaptive frequency cutoff between gravity and IG bands as described in Section 3.

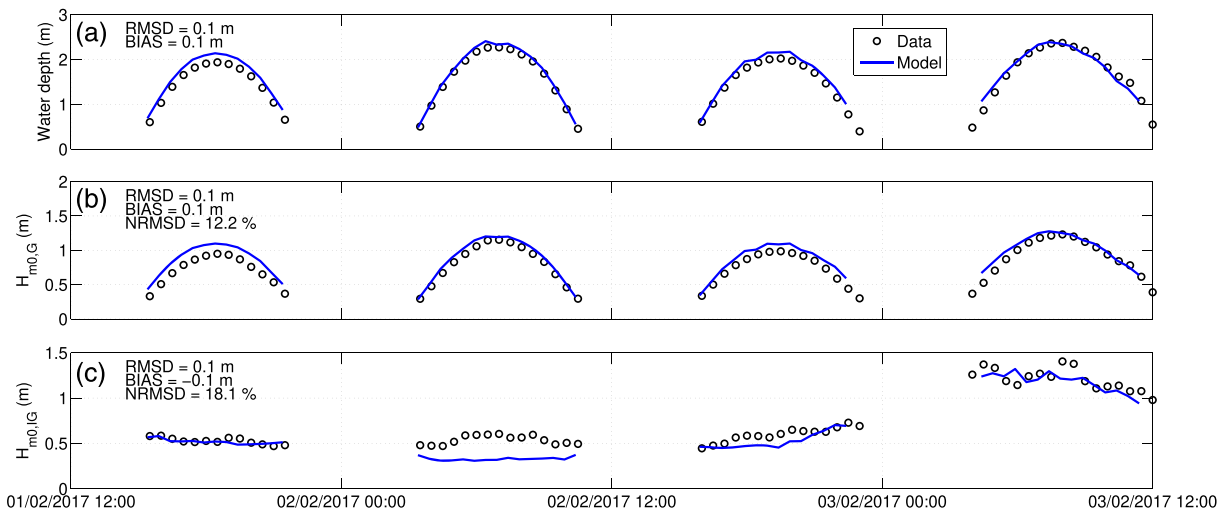


Figure 3. Modeled (blue line) against observed (black circle) water depth (a), H_{m0} in the gravity (b), and in the IG (c) bands at PT3/ADCP2.

$H_{m0,IG}$ are well reproduced by XBeach, except during the second tidal cycle where a 0.2 m negative bias can be observed (Figure 3), a problem that is also found at the ADCP1 (Figure 2c). Considering the whole set of intertidal sensors, $H_{m0,IG}$ are reproduced by XBeach with a RMSD of 0.14 m, which corresponds to a NRMSD of 20% (Figure 4b). To be more specific, $H_{m0,IG}$ are particularly underestimated when the incident short waves have a large directional spreading (i.e., $>35^\circ$, Figure 4b), which occurred mainly during the second tidal cycle (Figure 3). While discarding model results for such conditions, the RMSD drops to 0.08 m and the NRMSD to 11%, which corresponds to high predictive skills compared to previously published studies that provide a detailed validation of XBeach (e.g., Bertin & Olabarrieta, 2016; Lashley et al., 2018; Van Dongeren et al., 2013). The underestimation of IG waves for broad shortwave spectra is related to the original surfbeat

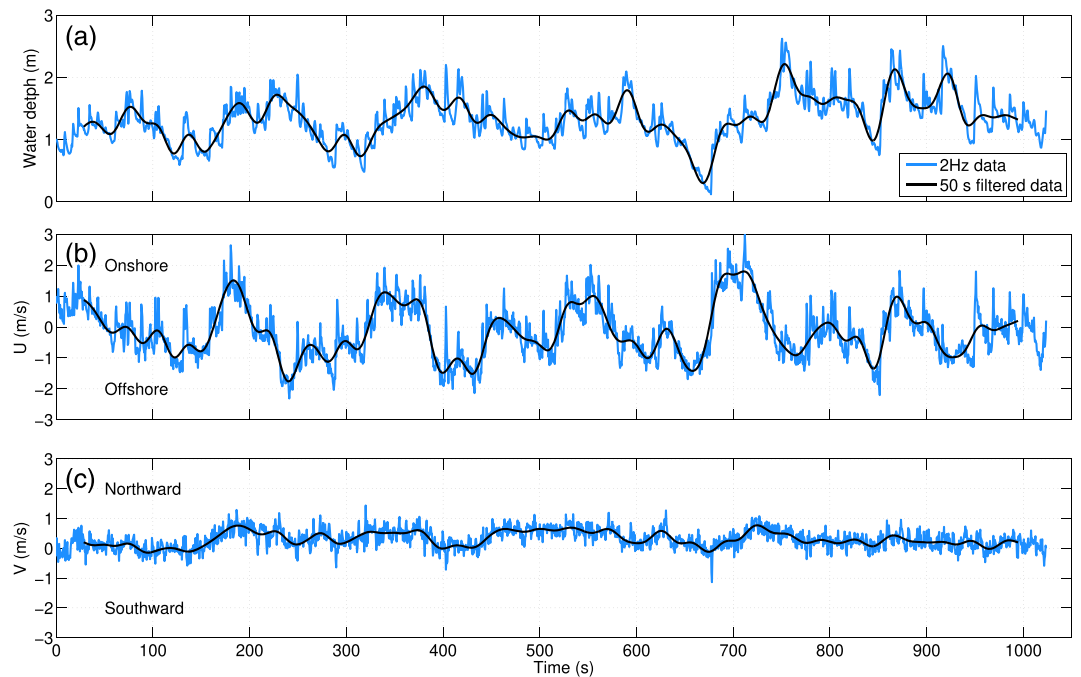


Figure 4. Modeled against observed H_{m0} in the gravity (a) and in the IG (b) bands, where symbol color corresponds to the directional spreading of the incident short waves at the open boundary of the modeled domain (Figure 1c).

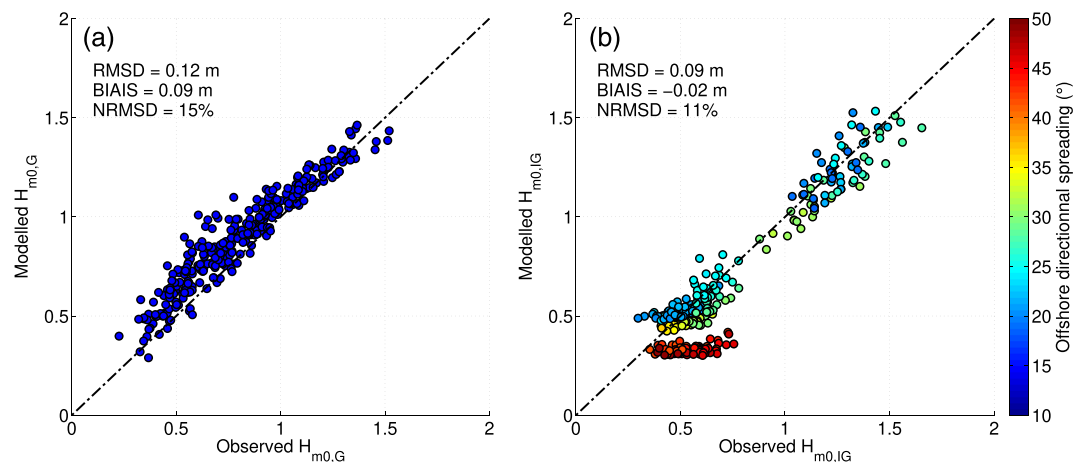


Figure 5. Time series of water depth (a), near bottom cross-shore (b), and longshore velocity (c) at 2 Hz (blue) and low-pass filtered (black), measured at the ADCP2/PT3 (Figure 1c) on the 3 February 2017 at 5h00.

approach of Xbeach, where the wave energy from different directional bins is simply added up, without considering the interference of the different wave components (Roelvink et al., 2018). To overcome this problem, Roelvink et al. (2018) recently proposed an alternative approach, where the mean wave directions are calculated first and the shortwave energy is then propagated along these directions. However, evaluating the recent improvements of XBeach is outside the scope of this study, focused on the physical processes associated with IG waves.

5.2. Frequency Repartition of IG Wave Energy

In order to investigate the evolution of the IG wave energy frequency repartition with a sufficient spectral resolution, we analyzed 3 hr-long time series of modeled and observed water depth, centered on the high tide of the last tidal cycle (storm Kurt). Incoming and outgoing modeled IG waves were separated using a Radon transform (Section 4.3), but the number of intertidal sensors was too limited to apply this technique to field measurements.

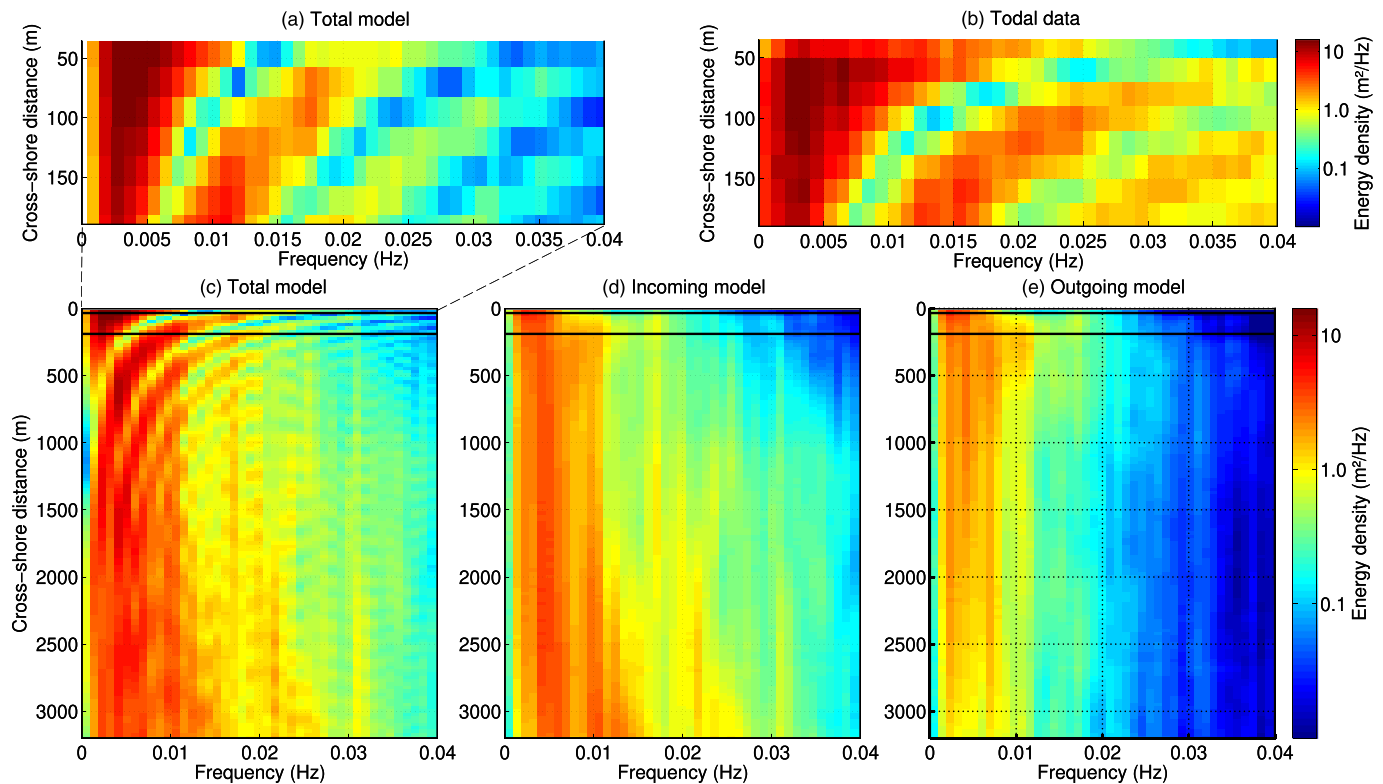


Figure 6. Spatio-frequential repartition of IG wave power spectral density modeled (a) and observed (b) for the total signals in the intertidal zone and modeled along the studied cross-shore transect for the total (c), the incoming (d), and the outgoing (e) signals.

Figures 6a and 6b show similarities between the modeled and the observed spatio-frequential patterns of IG wave energy in the intertidal zone, with a main peak between 0.01 and 0.015 Hz, a superharmonic peak around 0.02 and 0.025 Hz, and a subharmonic peak between 0.001 and 0.005 Hz. From the beach lower part to the beach upper part, these three peaks slide toward higher frequencies and the lower frequency one totally dominates the power density spectra along the shoreline. Such intriguing patterns were already observed in laboratory experiments of IG waves (Battjes et al., 2004; Buckley et al., 2018) and shortwaves (Martins et al., 2017) and are explained by interference between incoming and outgoing IG waves, creating nodes and antinodes, whose position with respect to the shoreline varies with the IG wave frequency and the bottom slope. Figures 6d and 6e corroborate this hypothesis and show that this pattern disappears in the modeled spectra corresponding to the incoming and outgoing signals. The analysis of the modeled spectra for the incoming signal (Figure 6d) reveals that, at the shoreface, IG wave energy is mostly located around a first peak at 0.01 Hz and a second broader peak centered around 0.005 Hz. A superharmonic secondary peak is also present around 0.02 Hz. Approaching the shoreline, IG wave energy at higher frequencies decreases while most of the energy is located between 0.002 and 0.006 Hz. The spectra of the outgoing signal (Figure 6e) suffer less transformation and, compared to the incoming signal, display much less energy at frequencies above 0.015 to 0.02 Hz.

This analysis was extended to the whole studied period based on the mean incoming IG wave period T_{m02,IG^+} (Figure 7a), computed from the incoming IG wave signal. For moderate-energy wave conditions, this figure shows that T_{m02,IG^+} first decreases from about 60 to 70 s in 10 m water depth to about 50 s in 2 m water depth. For a given location along the studied cross-shore profile, T_{m02,IG^+} exhibits therefore a substantial tidal modulation. In water depth less than 1 m, T_{m02,IG^+} increases back to 60–70 and even over 80 s at low tide (Figure 7). Under storm wave conditions (3 February 2017), a different behavior is observed, with a continuous increase in T_{m02,IG^+} from about 70 s in 10 m water depth to 90–100 s in 2 m water depth. In water depth less than 1 m, T_{m02,IG^+} further increases up to 120 s at low tide. The modeled temporal evolution of T_{m02,IG^+} fairly matches the observations at the location of the ADCP2 and ADV, with a RMSD of 8 s, corresponding to a 12% error.

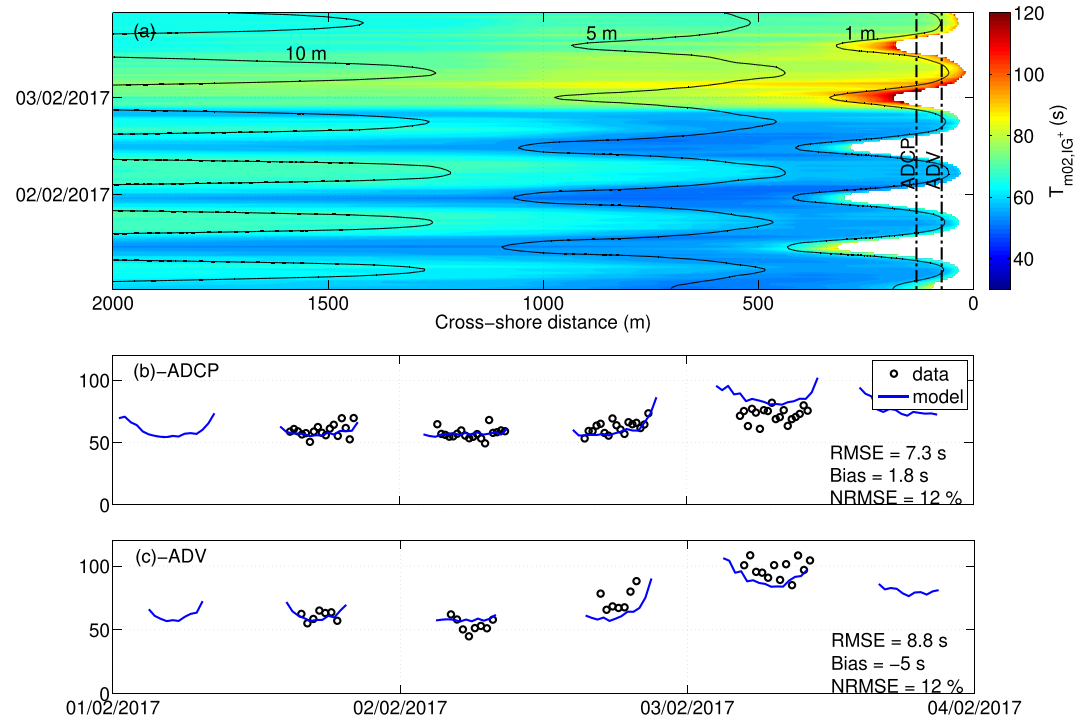


Figure 7. (a) Spatio-temporal repartition of incoming mean IG wave period T_{m02,IG^+} along the studied cross-shore transect. Modeled against observed time series of T_{m02,IG^+} and the ADCP2 (b) and the ADV (c).

5.3. Reflection

The comparison between observed and modeled reflection coefficient R^2 shows a good agreement in the intertidal zone, with a RMSD of 0.12, corresponding to a normalized error of about 15% (Figures 8b and 8c). Under moderate-energy incident short waves, both modeled and observed R^2 show a strong tidal modulation, with values below 0.2 at low tide and close to 1.0 at high tide, suggesting full reflection along the waterline. This tidal modulation substantially weakens under storm wave conditions, with R^2 above 0.5 at low tide along the waterline.

Such a tidal modulation of R^2 was already reported by Okihiro and Guza (1995), who explained the higher reflection at high tide by the steeper slope of the beach upper part. In the present study, the beach slope increases from about 1:100 in the lower part of the intertidal zone to 1:25, which could directly explain the observed tidal modulation of IG wave reflection. Battjes et al. (2004) proposed that IG wave reflection is related to a normalized beach slope parameter β_H , defined as

$$\beta_H = \frac{\beta}{\omega} \sqrt{\frac{g}{H}}, \quad (8)$$

where β is the beach slope, ω is the IG wave angular frequency, g is the gravitational acceleration, and H corresponds to the height of the incoming IG wave. According to these authors, a large reflection would occur for β_H substantially above unity. Considering incoming IG waves of height 0.5 m and frequency 0.01 Hz, β_H would increase from about 0.7 at low tide to 3.0 at high tide, which explains the observed tidal modulation of R^2 . Outside the surf zone, model results suggest R^2 well above unity at high tide, which was already observed in the field by Elgar et al. (1994) and Sheremet et al. (2002). These authors interpreted this behavior by the fact that IG waves were gaining energy between their sensors and the shoreline, before being reflected from a steep beach face.

6. Discussion

6.1. Generation Mechanisms

The IG waves observed during our field campaign correspond to the largest values reported in the literature (Ruessink, 2010; Fiedler et al., 2015; Inch et al., 2017), while our adaptive frequency cutoff to separate gravity

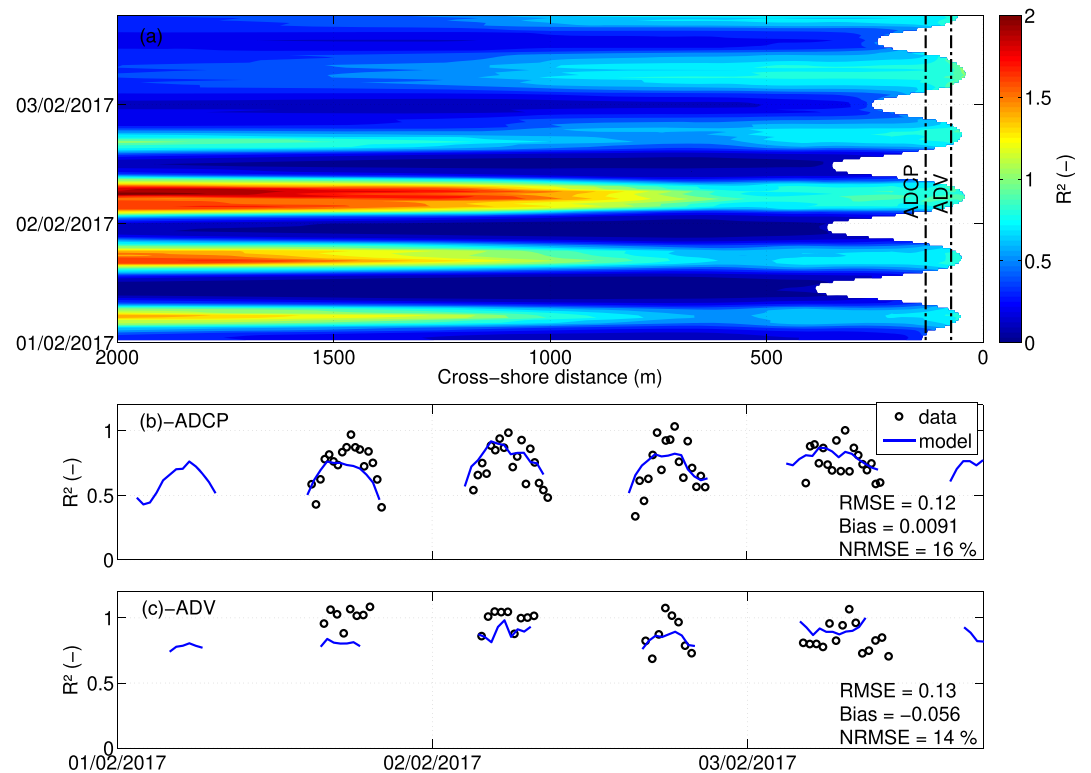


Figure 8. (a) Spatiotemporal variations of reflection coefficients R^2 computed over the studied period using a Radon transform (Radon, 1917) and modeled (blue) against observed (circles) time series of R^2 at the ADCP2 (b) and the ADV (c).

and IG bands is more conservative than the fixed frequency cutoff used in these studies. At gently sloping beaches, it is usually admitted that IG waves are generated through the bound wave mechanism (Battjes et al., 2004; Inch et al., 2017; Bertin et al., 2018).

Considering the analytical solution proposed by Hasselmann (1962) to compute the bound wave based on directional wave spectra, energy transfers from the gravity band to the IG band increase when the wave energy is large and distributed over narrow spectra. Therefore, the very energetic and narrow-banded swell associated with the storm Kurt would directly explain the development of such large IG waves. In order to verify this hypothesis, we compared the incoming IG wave heights $H_{m0,IG+}$ computed from our baseline simulation with those computed from simulations where only either the bound wave or the breakpoint mechanisms were represented (see Section 4.2). This comparison reveals only modest differences between the baseline simulation (Figure 9a) and the simulation where only the bound wave is considered (Figure 9b). Conversely, the simulation where only the breakpoint mechanism is considered (Figure 9c) shows much smaller IG waves, with $H_{m0,IG+}$ ranging from 0.1 to 0.2 m during first three tidal cycles and 0.4 m around the peak of the storm. This analysis confirms that IG waves were mostly generated through the bound wave mechanism, independently from the tidal phase or the incident shortwave energy.

In accordance with this first finding, the modeled incoming IG waves are negatively correlated with the short wave energy envelope (hereafter WEE, Figure 10a). Strongest correlations are found from the breaking point up to water depths of about 12 m, with coefficients ranging from -0.4 to -0.9 over the studied period (always significant at 95%, mean -0.54 ± 0.16). In more details, the strongest negative correlations are not found at zero lag, and incoming IG waves are lagging behind the WEE by a few seconds. Figure 10b shows the modeled spatio-temporal evolution of the normalized phase lag between incoming IG waves and the WEE, shifted by π for the sake of readability. For moderate-energy incident conditions, this phase lag continuously increases from about $\pi/20$ by 10 m water depth to about $\pi/5$ by 4 m water depth, which corresponds to the beginning of the surf zone. In the inner surf zone, the correlation cancels out and then switches to positive

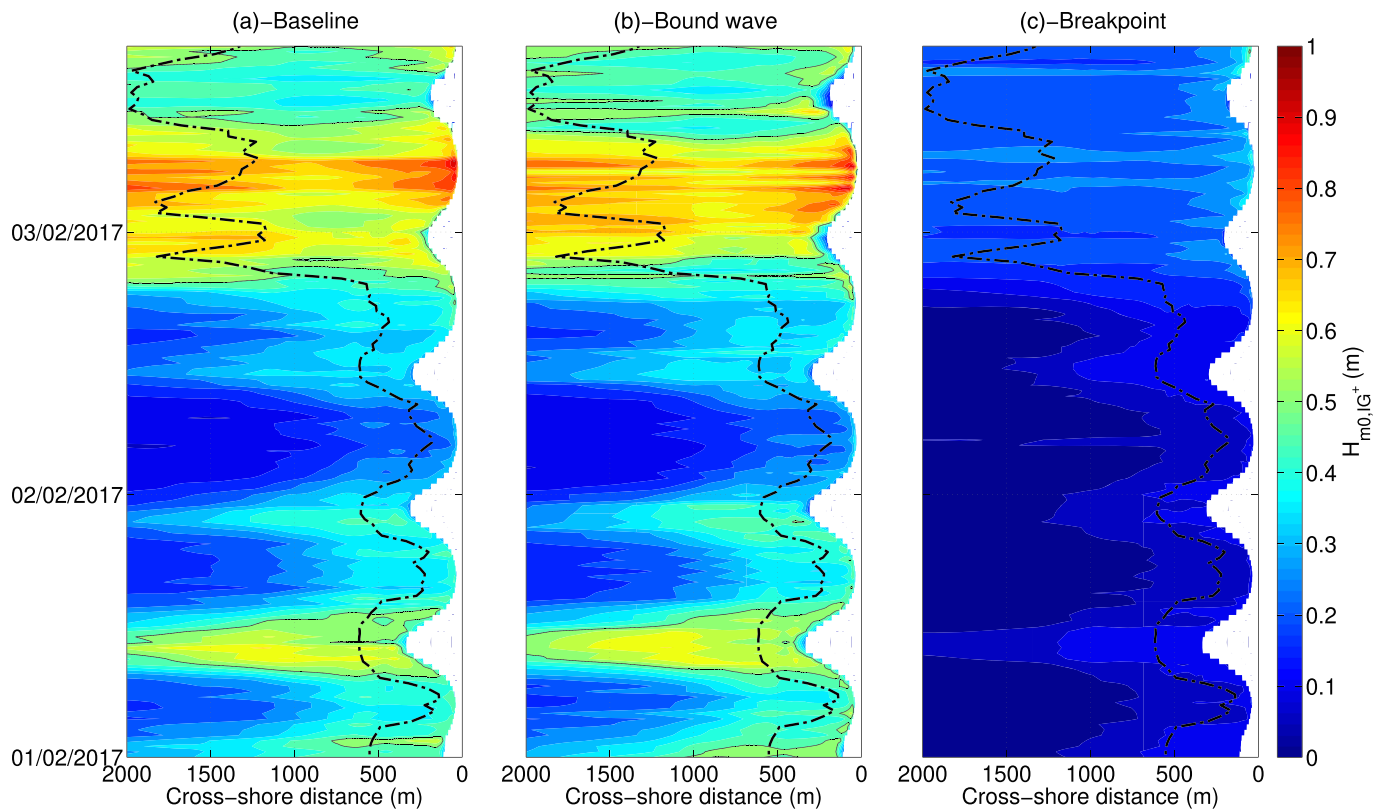


Figure 9. Modeled incoming IG wave height H_{m0,IG^+} in the baseline simulation (a), the bound wave case (b), and the breakpoint case (c). The black dotted line corresponds to the offshore limit of the surf zone, as defined in Section 4.2

(Figure 10a), due to the modulation of shortwave heights by IG waves, a process that is well documented (Guza et al., 1984; Inch et al., 2017; Tissier et al., 2015).

For storm wave conditions, a phase lag of about $\pi/10$ is already present by 10 m water depth (i.e., 3,000 m from the shoreline, Figure 10) and increases up to $\pi/5$ at the beginning of the inner surf zone. According to Van Dongeren et al. (2007), the presence of this phase lag enhances energy transfers from the short waves to the IG waves. Due to the gentle slope of the studied beach, this process is active over several kilometers under storm waves, which would explain the development of such large IG waves. However, our field data set entails several limitations that prevent from verifying these values. First, the ADCP1 was located more than 3,000 m from the intertidal profile, which implies travel times of IG waves ranging from 400 to 500 s, depending on the tidal phase. Over such a long distance/duration, IG waves suffer multiple transformations (see next sections) so that we were unable to correlate the offshore WEE with the IG waves at the intertidal sensors. Second, the width of the surf zone ranged from 200 m to more than 3,000 m, so that the intertidal sensors were always located inside the surf zone, where the correlation between IG waves and the WEE is biased positively as explained above.

6.2. Energy Transfers

In order to better explain the spatio temporal repartition of IG wave energy, source terms for nonlinear energy transfers between IG wave frequencies S_{nl} were computed using bispectra following Herbers et al. (2000) based on 24 hr-long runs corresponding to moderate-energy and storm conditions, both at low and high tide (Figure 11). This figure reveals that, at high tide, substantial energy transfers from frequencies in the range 0.01–0.03 Hz toward higher frequencies start to occur about 200 m from the shoreline (Figure 11a). At low tide, similar energy transfers occur but starting about 500 m from the waterline (Figure 11b). Surprisingly, the overall patterns of energy transfers are not very different for storm conditions, except that they affect lower IG wave frequencies (0.002 to 0.02 Hz) (Figures 11c and 11d). Note that for these high-energy cases, the overall patterns are shifted onshore because the mean water level is higher due to a larger wave setup.

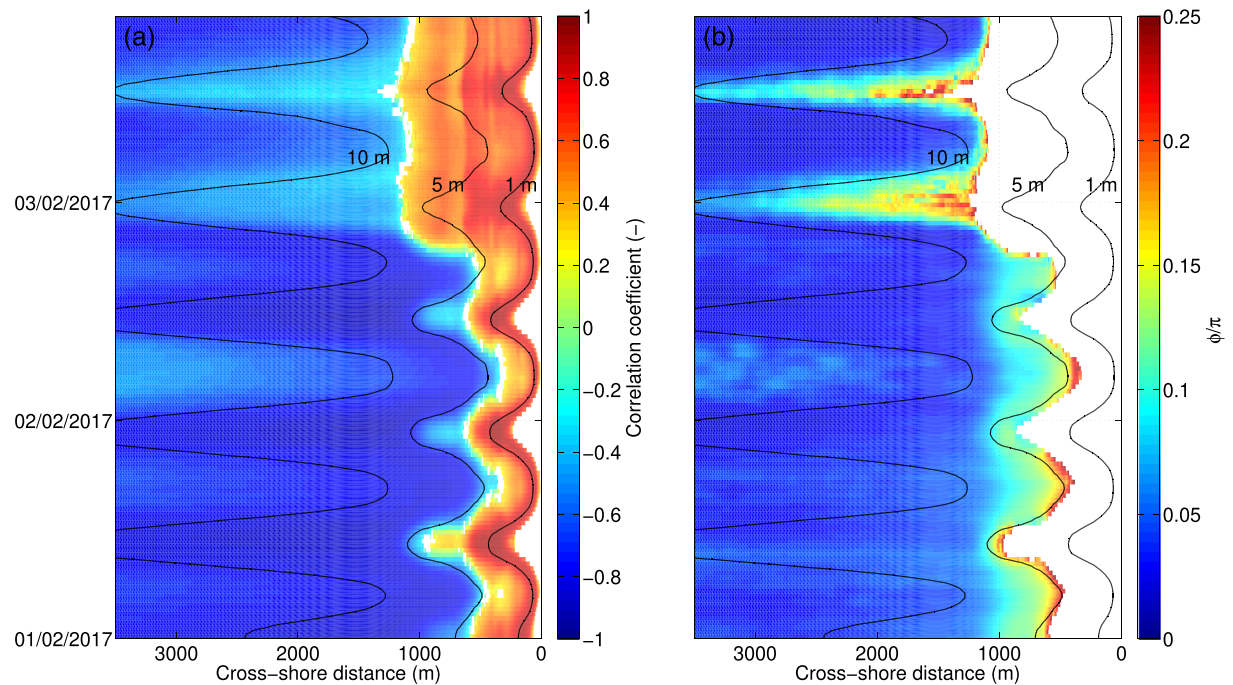


Figure 10. (a) Modeled correlation coefficient between the WEE and incoming IG waves and (b) modeled normalized phase lag, shifted by π (i.e., phase lag in radians shifted by π and then normalized by π) between incoming IG waves and the WEE. The black solid lines correspond to isolines of the mean water depth.

For moderate-energy wave conditions, the cross-shore evolution of S_{nl} (Figures 11a and 11b) suggests that the decrease in mean incoming IG wave period T_{m02,IG^+} with the water depth (Figure 7) and its subsequent tidal modulation is explained by energy transfers from principal components to higher harmonics via nonlinear coupling between triads. In shallow depth (i.e., less than 1 m), the increase in T_{m02,IG^+} is explained by the breaking of the higher-frequency IG waves, a process well supported at gently sloping beaches by field observations (De Bakker et al., 2014; Inch et al., 2017), laboratory experiments (Battjes et al., 2004; Van Dongeren et al., 2007; Padilla & Alsina, 2017), and numerical modeling (Ruju et al., 2012; De Bakker et al., 2016; Mendes et al., 2018). For storm wave conditions, a different situation occurs, where T_{m02,IG^+} continuously increases across the surf zone, so that T_{m02,IG^+} almost doubles from 10 m water depth to the shoreline (Figure 7). While the increase in T_{m02,IG^+} close to the shoreline can also be attributed to the breaking of the highest-frequency IG waves, an additional mechanism should be active in intermediate water depths where IG waves cannot break. Indeed, classical interactions between pairs of frequencies could hardly explain this behavior as the computation of S_{nl} reveals virtually no energy transfers toward very low frequencies, as for moderate-energy conditions (Figure 11). Analyzing field observations collected under storm waves at a steep rocky shore in western Brittany, Sheremet et al. (2014) reported the development of 300 s period IG waves along the shore. These authors applied a phase-resolving triad numerical model, which failed to reproduce such low-frequency IG waves and concluded that, as in the present study, it does not result from classical nonlinear triad interactions.

While the development of IG wave superharmonics at gently sloping beaches is reasonably well documented in the literature and explained through IG-IG nonlinear interactions (Elgar & Guza, 1985; De Bakker et al., 2015; De Bakker et al., 2016; Inch et al., 2017; Padilla & Alsina, 2017), the transfer of energy toward subharmonic frequencies received much less attention (De Bakker et al., 2016). To further look into this phenomenon, we analyzed timestack samples of modeled incoming free surface elevation, close to high tide under moderate energy (first tidal cycle) and storm waves (fourth tidal cycle, storm Kurt) (Figures 12a and 12b). On this figure, the troughs of the WEE were automatically detected at $x = 3,000$ m, and their location was then computed across the surf zone using the wave group velocity C_g , given by the linear wave theory and the representative frequency used in XBeach, which corresponds to $1/T_{m-1,0}$. For moderate energy, Figure 12a shows that IG wave crests 1 to 12 follow the WEE troughs, which means that they propagate at C_g and shows that they are bound to the wave groups. This behavior illustrates the dominance of the bound

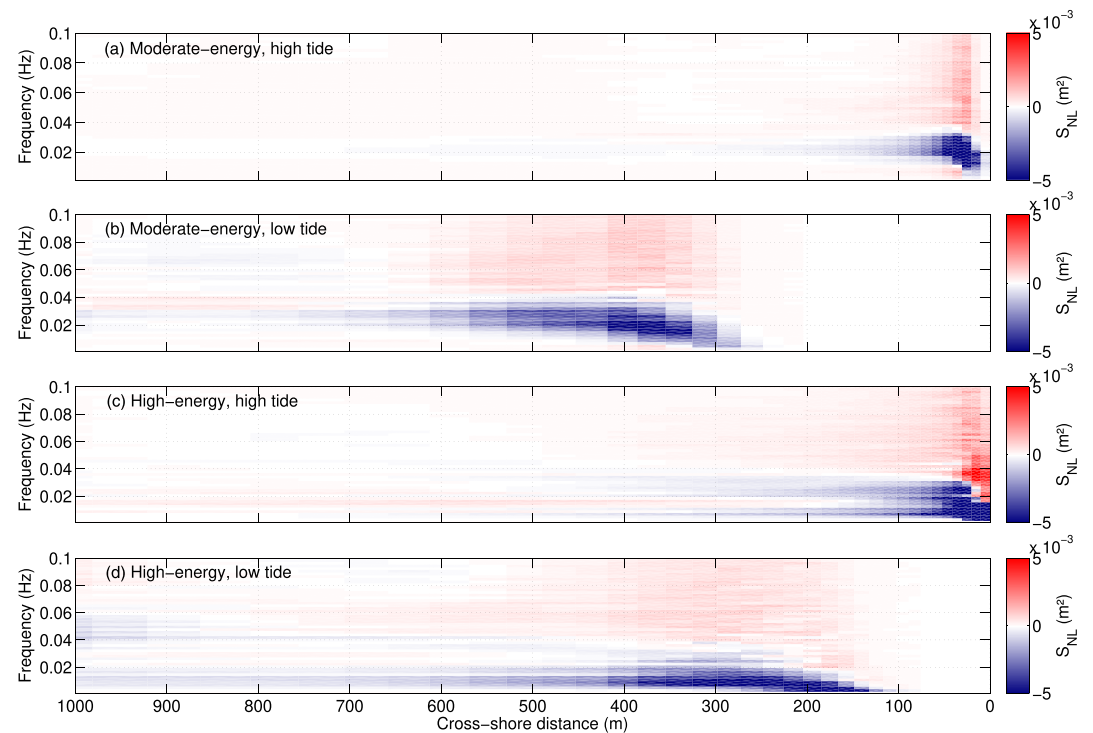


Figure 11. Source terms for nonlinear energy transfers between IG wave frequencies along the studied cross-shore profile computed for each frequency following Herbers et al. (2000) over 24 hr stationary runs for moderate and high-energy conditions, both at low and high tide.

wave mechanism in IG wave generation, as explained in Section 6.1. This situation strongly contrasts with storm wave conditions, where IG wave crests depart from the WEE troughs at different locations across the surf zone, meaning that they no longer travel at C_g but behave as free waves (Figure 12b). For instance, focusing on IG Wave Crests 1 to 4, Crest 1 seems bound to the wave group until $x = 500$ m, Crests 2 and 4 until $x = 2,300$ m, and Crest 3 until $x = 1,000$ m. Although less impressive, this process can also be observed for IG Wave Crests 6 and 10. Considering a mean water depth of 12 m at $x = 3,000$ m and a representative frequency of 0.064 Hz at the time of Figure 12b, bound IG waves propagate at $C_g = 9.8$ m s⁻¹ while free IG waves propagate at 10.84 m s⁻¹. Whereas such differences only represent 11% and further less when approaching the coastline, they result in travel-time differences ranging from 25 to 30 s once integrated over such a large surf zone. This allows the merging of individual crests into longer-period IG waves close to shore, as for instance Crest 2 with Crest 1, and Crests 4 with Crest 3 (Figure 12b). A closer look at the model results however suggests that the behavior of the near-shore IG wave field is more complex. For instance, new IG wave crests appear inside the surf zone, such as between Crests 2 and 3 at $x = 1,500$ m or between crests 11 and 12 at $x = 2,300$ m. As these IG wave crests coincide with the crests of the WEE, they may correspond to free IG waves generated through the breakpoint mechanism (Symonds et al., 1982). This hypothesis is supported by Figure 9c, which shows that the breakpoint mechanism is active 2,000 m from the shoreline under storm waves. Future studies based on extensive field measurements and/or phase resolving models will have to investigate the detailed processes responsible for IG wave merging and the possible contribution of breakpoint-generated free IG waves.

Small beach slopes and resulting wide surf zones exacerbate this process as it provides individual IG waves with more time to travel at slightly different speed and catch up with one another. Although it could not be evidenced here, a modulation of individual IG wave celerity by longer IG waves might also be possible in this region of the shoreface (Tissier et al., 2015), which would also promote the merging of individual waves. Ultimately, we propose that the interactions of incident bound and free IG waves along the gently sloping shoreface of Oléron Island explain the increase of the incoming IG wave period by a factor of 2 across the surf zone under storm waves (Figure 7). This mechanism also suggests that the frequency of IG waves close to shore is not only controlled by the shape of the incident short wave spectra (i.e., Hasselmann, 1962) but

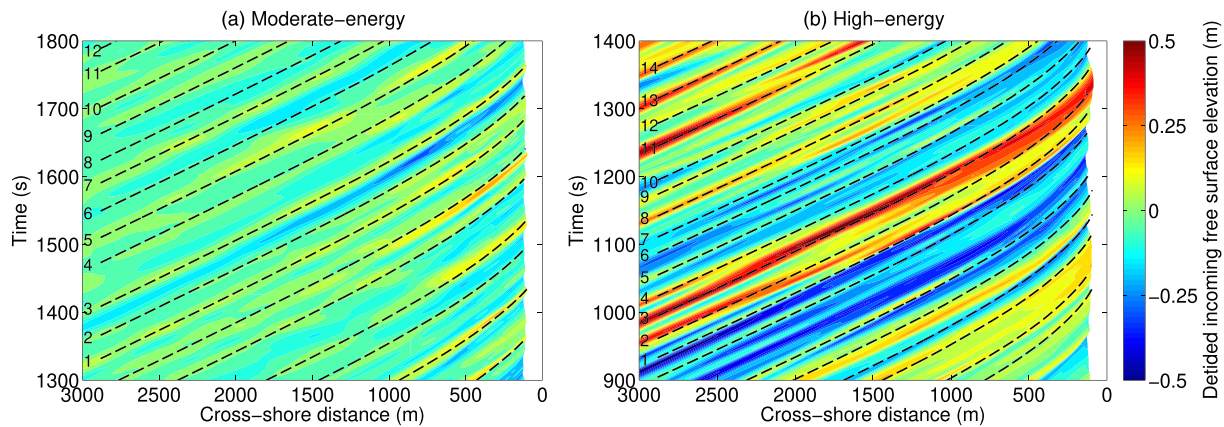


Figure 12. Timestack sample of modeled incident surface elevation (η_{IG+}) along the studied cross-shore transect around high tide for (a) moderate incident energy and (b) high-energy (storm Kurt). Numbers correspond to IG wave crests and the dashed black lines correspond to the troughs of the WEE, automatically detected at $x = 3,000$ m and then computed across the surf zone.

also by the width of the surf zone and hence the slope of the beach. This mechanism will have to be verified in the field, although instrumenting a surf zone several kilometer wide is very challenging.

6.3. Implications for Other Studies

In this study, we observed reflexion coefficient R^2 to be very high for a dissipative beach. For instance, De Bakker et al. (2014) and Inch et al. (2017) reported values for R^2 of the order of 0.5 or below for beaches of comparable mean bottom slope. The presence of a steeper upper beach in Saint Trojan can explain the higher reflexion observed at high tide, but not at low tide under storm wave conditions, where R^2 hardly drops below 0.5. We propose that the high reflection that we observe under storm waves is related to energy transfers toward subharmonic frequencies (Section 6.2), so that the resulting 200 to 300 s period IG waves are too long to suffer a substantial dissipation, even when propagating over a mild slope. Albeit not addressing the underlying mechanisms, a few other studies reported the development of IG waves with frequencies around 0.005 Hz under storm waves and suggested that they had a key role in runup (Ruggiero et al., 2004; Sheremet et al., 2014). Indeed, such low-frequency IG waves suffer less dissipation when propagating in shallow depth and may therefore propagate farther inland and induce larger damages in low-lying coastal zones compared to higher-frequency IG waves. The generation of low-frequency IG waves through merging of bound and free waves across wide surf zones appears therefore as a process of key importance and will have to be investigated at other sites, such as the very gently sloping coastlines of Bangladesh, which are extremely vulnerable to flooding under tropical hurricanes (Krien et al., 2017). This process should also be investigated at large estuaries and tidal inlets, where the ebb deltas can drive the development of kilometer-wide surf zones.

Besides, it is nowadays well admitted that free IG waves in the ocean are the main source of background-free oscillations of the solid earth, also referred to as "the hum of the Earth" (e.g., Rhie & Romanowicz, 2006; Webb, 2007). As better understanding the generation of the hum could help refining the use of microseism background signals to investigate the structure of the solid Earth, understanding IG wave reflection along the coast is of key importance. Correlating deep ocean pressure measurements with shortwave bulk parameters over the North Atlantic Ocean, Crawford et al. (2015) proposed that the main source for free IG wave generation was located between the Western part of the Iberic Peninsula and NW Africa, namely, because they display steep beaches. Our study suggests that strong reflection can also occur along dissipative beaches under storm waves, which will have to be considered in future studies on deep ocean IG waves.

7. Conclusions

This study aimed at improving our understanding of the generation and transformation of IG waves, combining an unpublished data set with numerical modeling. The development of exceptionally large IG waves was primarily explained by very energetic and narrow-banded incident shortwaves associated with the storm Kurt. The analysis of model results revealed that the bound wave mechanism was clearly dominant over

the breakpoint mechanisms in the generation of IG waves. Model results also showed that the gently sloping shoreface of the study area leads to the presence of a phase lag between IG waves and WEE over several kilometers under storm waves, which certainly enhanced IG wave generation through a dynamic shoaling, although our data set did not allow to further analyze this process. The XBeach modeling system was found capable of reproducing the generation and transformation of such IG waves, which is an important result as XBeach is becoming more and more popular while detailed hydrodynamic validations are lacking under storm conditions. Model results and field observations revealed that large energy transfers occur in the IG band across the surf zone, with the development of superharmonics but also the transfers of energy toward subharmonic frequencies. While the former behavior is reasonably well documented in the literature and explained by nonlinear coupling between triads, the latter was reported in a few studies only, and we propose that it is (at least partly) related to the merging of IG waves across the surf zone. According to our modeling results, IG wave merging seems to be related to the combination of free and bound IG waves in the surf zone, traveling at different celerities over a long distance. This mechanism will have to be verified on the field and is potentially of key importance under extreme storms, because low-frequency IG waves suffer little dissipation and may therefore propagate farther inland and induce larger damages compared to higher frequency IG waves. This mechanism also results in IG-wave reflection surprisingly high for a dissipative beach, which has implications for future studies on deep ocean IG waves.

Acknowledgments

This research was carried out in the scope of the Regional Chair Program EVEX, funded by the Region Poitou-Charentes (France). K. M. greatly acknowledges the financial support from the University of Bordeaux, through an International Postdoctoral Grant (Idex, nb. 1024R-5030). A. d.B. was partly funded by the program Prestige of Campus France (Grant Agreement PCOFUND-GA-2013-609102). We warmly thank the developing team of XBeach for making the code available. The processed field data and model input files required to run the XBeach simulations presented in this paper are available through a Zenodo repository (DOI:10.5281/zenodo.3753018).

References

- Aagaard, T., & Greenwood, B. (2008). Infragravity wave contribution to surf zone sediment transport—The role of advection. *Marine Geology*, *251*, 1–14. <https://doi.org/10.1016/j.margeo.2008.01.017>
- Almar, R., Michallet, H., Cienfuegos, R., Bonneton, P., Tissier, M. F. S., & Ruessink, B. G. (2014). On the use of the Radon Transform in studying nearshore wave dynamics. *Coastal Engineering*, *92*, 24–30. <https://doi.org/10.1016/j.coastaleng.2014.06.008>
- Baldock, T. E. (2012). Dissipation of incident forced long waves in the surf zone—implications for the concept of “bound” wave release at short wave breaking. *Coastal Engineering*, *60*(1), 276–285.
- Battjes, J. A., Bakkenes, H. J., Janssen, T. T., & van Dongeren, A. R. (2004). Shoaling of subharmonic gravity waves. *Journal of Geophysical Research*, *109*, C02009. <https://doi.org/10.1029/2003JC001863>
- Baumann, J., Chaumillon, E., Bertin, X., Schneider, J.-L., Guillot, B., & Schmutz, M. (2017). Importance of infragravity waves for the generation of washover deposits. *Marine Geology*, *391*, 20–35. <https://doi.org/10.1016/j.margeo.2017.07.013>
- Bertin, X., Castelle, B., Chaumillon, E., Butel, R., & Quique, R. (2008). Longshore transport estimation and inter-annual variability at a high-energy dissipative beach: Saint Trojan Beach, SW Oléron Island, France. *Continental Shelf Research*, *28*(10), 1316–1332. <https://doi.org/10.1016/j.csr.2004.12.004>
- Bertin, X., Chaumillon, E., Sottolichio, A., & Pedreros, R. (2005). Tidal inlet response to sediment infilling of the associated bay and possible implications of human activities: The Marennes-Oléron Bay and the Maumusson Inlet, France. *Continental Shelf Research*, *25*(9), 1115–1131. <https://doi.org/10.1016/j.csr.2004.12.004>
- Bertin, X., de Bakker, A., van Dongeren, A., Coco, G., Andro, G., Ardhuin, F., et al. (2018). Infragravity waves: From driving mechanisms to impacts. *Earth-Science Reviews*, *177*, 774–799. <https://doi.org/10.1016/j.earscirev.2018.01.002>
- Bertin, X., Li, K., Roland, A., & Bidlot, J.-R. (2015). The contribution of short-waves in storm surges: Two case studies in the Bay of Biscay. *Continental Shelf Research*, *96*, 1–15. <https://doi.org/10.1016/j.csr.2015.01.005>
- Bertin, X., Mendes, D., Martins, K., Fortunato, A. B., & Lavaud, L. (2019). The closure of a shallow tidal inlet promoted by infragravity waves. *Geophysical Research Letters*, *46*, 6804–6810. <https://doi.org/10.1029/2019GL083527>
- Bertin, X., & Olabarrieta, M. (2016). Relevance of infragravity waves at a wave-dominated inlet. *Journal of Geophysical Research*, *212*, 5418–5435. <https://doi.org/10.1002/2015JC011444>
- Biesel, F. (1952). Équations générales au second ordre de la houle irrégulière. *La Houille Blanche*, *7*(3), 372–376. <https://doi.org/10.1051/lhb/1952033>
- Bishop, C. T., & Donelan, M. A. (1987). Measuring waves with pressure transducers. *Coastal Engineering*, *11*, 309–328. [https://doi.org/10.1016/0378-3839\(87\)90031-7](https://doi.org/10.1016/0378-3839(87)90031-7)
- Buckley, M. L., Lowe, R. J., Hansen, J. E., van Dongeren, A. R., & Storlazzi, C. D. (2018). Mechanisms of wave-driven water level variability on reef-fringed coastlines. *Journal of Geophysical Research: Oceans*, *123*, 3811–3831. <https://doi.org/10.1029/2018JC013933>
- Crawford, W., Ballu, V., Bertin, X., & Karpytchev, M. (2015). The sources of deep ocean infragravity waves observed in the North Atlantic Ocean. *Journal of Geophysical Research*, *120*, 5120–5133. <https://doi.org/10.1002/2014JC010657>
- De Bakker, A. T. M., Brinkkemper, J. A., van der Steen, F., Tissier, M. F. S., & Ruessink, B. G. (2016). Cross-shore sand transport by infragravity waves as a function of beach steepness. *Journal of Geophysical Research: Earth Surface*, *121*, 1786–1799. <https://doi.org/10.1002/2016JF003878>
- De Bakker, A. T. M., Herbers, T. H. C., Smit, P. B., Tissier, M. F. S., & Ruessink, B. G. (2015). Nonlinear infragravity-wave interactions on a gently sloping laboratory beach. *Journal of Physical Oceanography*, *45*(2), 589–605. <https://doi.org/10.1175/JPO-D-14-0186.1>
- De Bakker, A. T. M., Tissier, M. F. S., Marieu, V., Sénéchal, N., Rujju, A., Lara, J., & Ruessink, B. G. (2013). Infragravity wave propagation and dissipation on a low-sloping laboratory beach. In *Proc. 7th int. conf. on coastal dynamics*, (pp. 443–452). Arcachon, France.
- De Bakker, A. T. M., Tissier, M. F. S., & Ruessink, B. G. (2014). Shoreline dissipation of infragravity waves. *Continental Shelf Research*, *72*, 73–82. <https://doi.org/10.1016/j.csr.2013.11.013>
- De Bakker, A. T. M., Tissier, M. F. S., & Ruessink, B. G. (2016). Beach steepness effects on nonlinear infragravity-wave interactions: A numerical study. *Journal of Geophysical Research*, *121*, 554–570. <https://doi.org/10.1002/2015JC011268>
- Elgar, S., & Guza, R. T. (1985). Observations of bispectra of shoaling surface gravity waves. *Journal of Fluid Mechanics*, *161*, 425–448. <https://doi.org/10.1017/S0022112085003007>
- Elgar, S., Herbers, T. H. C., & Guza, R. T. (1994). Reflection of ocean surface gravity waves from a natural beach. *Journal of Physical Oceanography*, *24*, 1503–1511. [https://doi.org/10.1175/1520-0485\(1994\)024<1503:ROOSGW>2:0:CO;2](https://doi.org/10.1175/1520-0485(1994)024<1503:ROOSGW>2:0:CO;2)

- Elgar, S., Herbers, T. H. C., Okihiro, M., Oltman-Shay, J., & Guza, R. T. (1992). Observations of infragravity waves. *Journal of Geophysical Research*, 97(C10), 15,573–15,577. <https://doi.org/10.1029/92JC01316>
- Fiedler, J. W., Brodie, K. L., McNinch, J. E., & Guza, R. T. (2015). Observations of runup and energy flux on a low-slope beach with high-energy, long-period ocean swell. *Geophysical Research Letters*, 42, 9933–9941. <https://doi.org/10.1002/2015GL066124>
- Guérin, T., Bertin, X., Coulombier, T., & de Bakker, A. (2018). Impacts of wave-induced circulation in the surf zone on wave setup. *Ocean Modelling*, 123, 86–97. <https://doi.org/10.1016/j.ocemod.2018.01.006>
- Guedes, M. C., Bryan, K. R., & Coco, G. (2013). Observations of wave energy fluxes and swash motions on a low-sloping, dissipative beach. *Journal of Geophysical Research*, 118, 3651–3669. <https://doi.org/10.1002/jgrc.20267>
- Guérin, T., de Bakker, A., & Bertin, X. (2019). On the bound wave phase lag. *Fluids*, 4, 152. <https://doi.org/10.3390/uids4030152>
- Guza, R. T., & Thornton, E. B. (1982). Swash oscillations on a natural beach. *Journal of Geophysical Research*, 87, 483–491. <https://doi.org/10.1029/JC087iC01p00483>
- Guza, R. T., & Thornton, E. B. (1985). Observations of surf beat. *Journal of Geophysical Research*, 87, 483–491. <https://doi.org/10.1029/JC090iC02p03161>
- Guza, R. T., Thornton, E. B., & Holman, R. A. (1984). Swash on steep and shallow beaches, *Proceedings of the 19th international conference on coastal engineering* pp. 708–723. Houston, Texas: ASCE.
- Hamm, L., & Peronnard, C. (1997). Wave parameters in the nearshore: A clarification. *Coastal Engineering*, 32(2-3), 119–135. [https://doi.org/10.1016/S0378-3839\(97\)81746-2](https://doi.org/10.1016/S0378-3839(97)81746-2)
- Hasselmann, K. (1962). On the non-linear energy transfer in a gravity-wave spectrum Part 1. General theory. *Journal of Fluid Mechanics*, 12(04), 481–500. <https://doi.org/10.1017/S0022112062000373>
- Hasselmann, K., Munk, W., & MacDonald, G. (1963). Bispectra of ocean waves, *Time Series Analysis*. New York: John Wiley.
- Herbers, T. H. C., Elgar, S., & Guza, R. T. (1994). Infragravity-frequency (0.005–0.05 Hz) motions on the shelf. Part I: Forced waves. *Journal of Physical Oceanography*, 24, 917–927. [https://doi.org/10.1175/1520-0485\(1994\)024<0917:IFHMOT>2:0:CO;2](https://doi.org/10.1175/1520-0485(1994)024<0917:IFHMOT>2:0:CO;2)
- Herbers, T. H. C., Russnogle, N. R., & Elgar, S. (2000). Spectral energy balance of breaking waves within the surf zone. *Journal of Physical Oceanography*, 30, 2723–2737.
- Huntley, D. A., Guza, R. T., & Thornton, E. B. (1981). Field observations of surf beat: 1. Progressive edge waves. *Journal of Geophysical Research*, 86(C7), 6451–6466. <https://doi.org/10.1029/JC086iC07p06451>
- Inch, K., Davidson, M., Masselink, G., & Russell, P. (2017). Observations of nearshore infragravity wave dynamics under high energy swell and wind-wave conditions. *Continental Shelf Research*, 138, 19–31. <https://doi.org/10.1016/j.csr.2017.02.010>
- Janssen, T. T., Battjes, J. A., & van Dongeren, A. R. (2003). Long waves induced by short-wave groups over a sloping bottom. *Journal of Geophysical Research*, 108, 3252. <https://doi.org/10.1029/2002JC001515>
- Krien, Y., Testut, L., Islam, A. K. M. S., Bertin, X., Durand, F., Mayet, C., et al. (2017). Towards improved storm surge models in the northern Bay of Bengal. *Continental Shelf Research*, 135, 58–73.
- Lashley, C. H., Roelvink, D., van Dongeren, A., Buckley, M. L., & Lowe, R. (2018). Nonhydrostatic and surfbeat model predictions of extreme wave run-up in fringing reef environments. *Coastal Engineering*, 137, 11–27. <https://doi.org/10.1016/j.coastaleng.2018.03.007>
- Lin, Y.-H., & Hwung, H.-H. (2012). Infra-gravity wave generation by the shoaling wave groups over beaches. *China Ocean Engineering*, 26, 1–18. <https://doi.org/10.1007/s13344-012-0001-9>
- List, J. H. (1992). A model for the generation of two-dimensional surf beat. *Journal of Geophysical Research*, 97(C4), 5623–5635.
- Longuet-Higgins, M. S., & Stewart, R. W. (1962). Radiation stress and mass transport in gravity waves, with application to surf beats. *Journal of Fluid Mechanics*, 13(4), 481–504. <https://doi.org/10.1017/S0022112062000877>
- Martins, K., Blenkinsopp, C. E., Almar, R., & Zang, J. (2017). The influence of swash-based reflection on surf zone hydrodynamics: A wave-by-wave approach. *Coastal Engineering*, 122, 27–43.
- Masselink, G. (1995). Group bound long waves as a source of infragravity energy in the surf zone. *Continental Shelf Research*, 15(13), 1525–1547. [https://doi.org/10.1016/0278-4343\(95\)00037-2](https://doi.org/10.1016/0278-4343(95)00037-2)
- Mendes, D., Fortunato, A. B., Bertin, X., Martins, K., Lavaud, L., Silva, A. N., et al. (2020). Importance of infragravity waves in a wave-dominated inlet under storm conditions. *Continental Shelf Research*, 192, 104,026.
- Mendes, D., Pinto, J. P., Pires-Silva, A. A., & Fortunato, A. B. (2018). Infragravity wave energy changes on a dissipative barred beach: A numerical study. *Coastal Engineering*, 140, 136–146. <https://doi.org/10.1016/j.coastaleng.2018.07.005>
- Nicolae-Lerma, A., Bulteau, T., Lecacheux, S., & Idier, D. (2015). Spatial variability of extreme wave height along the atlantic and channel french coast. *Ocean Engineering*, 97(-), 175–185. <https://doi.org/10.1016/j.oceaneng.2015.01.015>
- Okihiro, M., & Guza, R. T. (1995). Infragravity energy modulation by tides. *Journal of Geophysical Research*, 100(C8), 16,143–16,148. <https://doi.org/10.1029/95JC01545>
- Padilla, E. M., & Alsina, J. M. (2017). Transfer and dissipation of energy during wave group propagation on a gentle beach slope. *Journal of Geophysical Research: Oceans*, 122, 6773–6794. <https://doi.org/10.1002/2017JC012703>
- Pomeroy, A., Lowe, R., Symonds, G., Van Dongeren, A., & Moore, C. (2012). The dynamics of infragravity wave transformation over a fringing reef. *Journal of Geophysical Research*, 117, C11022. <https://doi.org/10.1029/2012JC008310>
- Radon, J. (1917). Über die bestimmung von funktionen durch ihre integralwerte längs gewisser mannigfaltigkeiten. *Berichte Sächsische Akademie der Wissenschaften, Leipzig, Math.-Phys.Kl.*, 69, 262–267.
- Raubenheimer, B., & Guza, R. T. (1996). Observations and predictions of run-up. *Journal of Geophysical Research*, 101, 25,575–25,587.
- Rawat, A., Arduin, F., Ballu, V., Crawford, W., Corela, C., & Aujan, J. (2014). Infragravity waves across the oceans. *Geophysical Research Letters*, 41, 7957–7963. <https://doi.org/10.1002/2014GL061604>
- Reniers, A. J. H. M., van Dongeren, A. R., Battjes, J. A., & Thornton, E. B. (2002). Linear modelling of infragravity waves during Delilah. *Journal of Geophysical Research*, 107, 3137. <https://doi.org/10.1029/2001JC001083>
- Rhie, J., & Romanowicz, B. (2006). A study of the relation between ocean storms and the Earth-s hum. *Geochemistry Geophysics Geosystems*, 7, Q10004. <https://doi.org/10.1029/2006GC001274>
- Roelvink, J. A. (1993a). Dissipation in random wave groups incident on a beach. *Coastal Engineering*, 19(1-2), 127–150. [https://doi.org/10.1016/0378-3839\(93\)90021-Y](https://doi.org/10.1016/0378-3839(93)90021-Y)
- Roelvink, J. A. (1993b). Surf beat and its effect on cross-shore profiles (Ph.D. Thesis).
- Roelvink, D., McCall, R., Mehvar, S., Nederhoff, K., & Dastgheib, A. (2018). Improving predictions of swash dynamics in XBeach: The role of groupiness and incident-band runup. *Coastal Engineering*, 134, 103–123. <https://doi.org/10.1016/j.coastaleng.2017.07.004>
- Roelvink, D., Reniers, A., van Dongeren, A., van Thiel de Vries, J., McCall, R., & Lescinski, J. (2009). Modelling storm impacts on beaches, dunes and barrier islands. *Coastal Engineering*, 56, 1133–1152. <https://doi.org/10.1016/j.coastaleng.2009.08.006>
- Roelvink, J. A., & Stive, M. F. J. (1989). Bar-generating cross-shore flow mechanisms on a beach. *Journal of Geophysical Research*, 94(C4), 4785–4800.

- Ruessink, B. G. (2010). Observations of turbulence within a natural surf zone. *Journal of Physical Oceanography*, *40*, 2696–2712. <https://doi.org/10.1175/2010JPO4466.1>
- Ruessink, B. G., Houwman, K. T., & Hoekstra, P. (1998). The systematic contribution of transporting mechanisms to the cross-shore sediment transport in water depths of 3 to 9 m. *Marine Geology*, *152*, 295–324. [https://doi.org/10.1016/S0025-3227\(98\)00133-9](https://doi.org/10.1016/S0025-3227(98)00133-9)
- Ruessink, B. G., Kleinhans, M. G., & Van den Beukel, P. G. L. (1998). Observations of swash under highly dissipative conditions. *Journal of Geophysical Research*, *103*, 3111–3118. <https://doi.org/10.1029/97JC02791>
- Ruggiero, P., Holman, R. A., & Beach, R. A. (2004). Wave run-up on a high-energy dissipative beach. *Journal of Geophysical Research*, *109*(6), C06025. <https://doi.org/10.1029/2003JC002160>
- Ruggiero, P., Komar, P. D., McDougal, W. G., Marra, J. J., & Beach, R. A. (2001). Wave runup, extreme water levels and the erosion of properties backing beaches. *Journal of Coastal Research*, *17*(2), 407–419.
- Ruju, A., Lara, J. L., & Losada, I. J. (2012). Radiation stress and low-frequency energy balance within the surf zone: A numerical approach. *Coastal Engineering*, *68*, 44–55. <https://doi.org/10.1016/j.coastaleng.2012.05.003>
- Russell, P. (1993). Mechanisms for beach erosion during storm. *Continental Shelf Research*, *13*, 1243–1265. [https://doi.org/10.1016/0278-4343\(93\)90051-X](https://doi.org/10.1016/0278-4343(93)90051-X)
- Sénéchal, N., Coco, G., Bryan, K. R., & Holman, R. A. (2011). Wave runup during extreme storm conditions. *Journal of Geophysical Research*, *116*, C07032. <https://doi.org/10.1029/2010JC006819>
- Saha, S., Moorthi, S., Pan, H.-L., Wu, X., Wang, J., Nadiga, S., et al. (2010). The NCEP climate forecast system reanalysis. *Bulletin of the American Meteorological Society*, *91*(8), 1015–1057. <https://doi.org/10.1175/2010BAMS3001.1>
- Sheremet, A., Guza, R. T., Elgar, S., & Herbers, T. H. C. (2002). Observations of nearshore infragravity waves: Seaward and shoreward propagating components. *Journal of Geophysical Research*, *107*(C8), 3095. <https://doi.org/10.1029/2001JC000970>
- Sheremet, A., Staples, T., Ardhuin, F., Suanez, S., & Fichaut, B. (2014). Observations of large infragravity runup at Banneg Island, France. *Geophysical Research Letters*, *41*, 976–982. <https://doi.org/10.1002/2013GL058880>
- Smit, P. B., Janssen, T. T., Herbers, T. H. C., Taira, T., & Romanowicz, B. A. (2018). Infragravity wave radiation across the shelf break. *Journal of Geophysical Research: Oceans*, *123*, 4483–4490. <https://doi.org/10.1029/2018JC013986>
- Symonds, G., Huntley, D., & Bowen, A. J. (1982). Two-dimensional surf beat: Long wave generation by a time-varying breakpoint. *Journal of Geophysical Research*, *87*, 492–498.
- Tissier, M., Bonneton, P., Michallet, H., & Ruessink, B. G. (2015). Infragravity-wave modulation of short-wave celerity in the surf zone. *Journal of Geophysical Research: Oceans*, *120*(10), 6799–6814. <https://doi.org/10.1002/2015JC010708>
- Tolman, H. L. (2009). User manual and system documentation of WAVEWATCH III version 3.14, (276), 194 pp.
- Van Dongeren, A., Battjes, J., Janssen, T., van Noorloos, J., Steenhauer, K., Steenbergen, G., & Reniers, A. (2007). Shoaling and shoreline dissipation of low-frequency waves. *Journal of Geophysical Research*, *112*. <https://doi.org/10.1029/2006JC003701>
- Van Dongeren, A. R., Lowe, R., Pomeroy, A., Trang, D. M., Roelvink, D., Symonds, G., & Ranasinghe, R. (2013). Numerical modeling of low-frequency wave dynamics over a fringing coral reef. *Coastal Engineering*, *73*, 178–190. <https://doi.org/10.1016/j.coastaleng.2012.11.004>
- Webb, S. C. (2007). The Earth's 'hum' is driven by ocean waves over the continental shelves. *Nature*, *445*, 754–756. <https://doi.org/10.1038/nature05536>
- Yoo, J., Fritz, H. M., Haas, K. A., Work, P. A., & Barnes, C. F. (2011). Depth inversion in the surf zone with inclusion of wave nonlinearity using video-derived celerity. *Journal of Waterway, Port, Coastal and Ocean Engineering*, *137*(2), 95–106. [https://doi.org/10.1061/\(ASCE\)WW.1943-5460.0000068](https://doi.org/10.1061/(ASCE)WW.1943-5460.0000068)